Effects of Clamping on the Laser Forming Process

A. J. Birnbaum
e-mail: ajb2118@columbia.edu

P. Cheng

Y. L. Yao

Department of Mechanical Engineering,
Columbia University,
New York, NY 10027

Although considerable effort has gone into characterizing the laser forming process in terms of process parameters and conditions, there has been little emphasis on the effects of the mechanical and thermal constraints introduced by the clamping method utilized for a desired application. This research suggests means for investigating and predicting the resulting geometry of a specimen due to laser operation in close proximity to an array of imposed thermo-mechanical constraints for both the single and multiple scan cases; specifically, the resulting average bending angle as well as bending angle variations throughout the part. This is accomplished by initially only considering these effects on the thermal field. Conclusions are then drawn about the nature of the mechanical effects. These conclusions are validated through numerical simulation as well as physical experimentation. An analytical solution of the thermal problem is also presented for further validation of the temperature field as a constrained edge is approached.
[DOI: 10.1115/1.2375140]

1 Introduction

The laser forming process involves the local/concentrated input of energy through the use of a defocused laser, moving at a relative velocity to a thin-sheet work piece of varying geometric complexity. This local energy input results in a nonuniform transient temperature distribution, giving rise to thermally induced stresses, strains, and permanent deformations. Through proper control over process parameters such as laser velocity, power, beam spot size, path geometry, and clamping method, final part geometries as well as material characteristics may be controlled to an acceptable degree of accuracy.

Laser forming, a nontraditional manufacturing process, does not require any externally applied forces to generate desired forms. This is a significant advantage it has over its traditional counterparts, as the hard tooling process has been eliminated from the overall process flow. This also introduces a considerable degree of flexibility, as hard tooling has in effect been replaced by virtual means, in that process parameters, as well as path geometry, may be altered at any time to create totally new forming conditions.

Much effort has been made in characterizing the underlying mechanisms for the process. Vollertsen [1] has identified three main mechanisms which give rise to various types of deformation, while Mucha [2] provided analytical formulations of the mechanical process, and Bao and Yao [3] address final deformation characteristics, specifically edge effects which are highly relevant to this research.

Though much has been determined with respect to the underlying mechanisms for deformation as well as the aggregate effects of varying process parameters, little effort has been put forth in studying the effects of part fixturing. Although fixturing requirements are loose in laser forming because, as mentioned above, it requires no external forces or hard tooling, the work piece still needs to be properly located/oriented and kept stable while deformation is taking place. Work holding is seen as a major issue for many traditional manufacturing processes. Fixture design and analysis, as well as its impact on the process to which it is applied, have all received much attention. Methods for increasing the efficiency of overall process flow with respect to effective work holding have also been explored [4]. Work holding "ideologies" like the 3-2-1 locating scheme have even been developed, where each number in the 3-2-1 sequence represents the number of constraining points; 3 points defining a plane, 2, a line and 1 additional point serving to fully constrain the part. In many manufacturing processes, fixturing method can have significant effects on post-process material characteristics including residual stresses, microstructure, warpage, and distortion. For example, Wang and Pelinescu [5], through a contact analysis, studied the work-piece-fixture contact force for a general clamp-support-locator configuration, Karafillis and Boyce [6] examined the post-process "spring back" effect in sheet metal forming, while Roy [7] investigated work-piece stability issues for a virtual disturbance on a general fixture-work-piece configuration within an automated fixture design environment.

Although, as mentioned above, laser forming is an extremely flexible process in that no hard tooling is required, a method for maintaining desired part location and orientation is still required. However, the degree to which parts may be constrained is also quite flexible. For example, the V-block configuration used by Edwardson [8] consists simply of a platform which the part lays on, with a V-shape cutout to freely allow bending deformation of thin sheet coupons. However, this approach is most suited toward simple straight line forming. Jones [9] employs the use of a water, cooling bed, which also essentially serves as a platform for part support, but is given total freedom to deform as the platform itself is flexible and free to deform. However, this arrangement may not be convenient for industrial applications due to the added task of the handling of a working fluid. In most cases reported to date, a method such as edge or corner clamping is employed to provide the necessary part orientation with respect to the laser; Hu et al. [10] and Li and Yao [11].

In terms of application, the two practical methods that have emerged require that either the part be fixed while the laser moves relative to it or the reverse situation where the laser is static and the part is translated or rotated by an *x-y* stage or robotic manipulation through predetermined paths. The research herein examines in depth the effects of both the method of fixturing utilized as well as the effects of laser operation in close proximity to an applied external constraint, such as an edge clamp. Lee [12] has recognized the potential impact of operating close to an applied external constraint, such as an edge clamp. Although he does not specifically explore these issues, he does go about choosing an operating distance that he deems sufficiently great from the clamp so as to minimize these potential effects. This study also examines these effects for an array of process parameters, thereby providing a set

Contributed by the Manufacturing Engineering Division of ASME for publication in the JOURNAL OF MANUFACTURING SCIENCE AND ENGINEERING. Manuscript received August 2, 2005; final manuscript received June 5, 2006. Review conducted by K. Rajurkar.

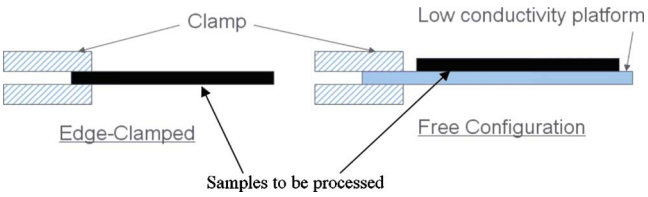

Fig. 1 Schematic of clamped and unclamped configurations

of practical guidelines for application by taking these factors into account when determining laser path geometries and heating conditions.

2 Overview of Approach

This research examines the edge-clamped, and the so-called free case, where there is no externally applied constraint other than the provision of a flat surface for support (Fig. 1). With the assumption that the process is sequentially coupled, i.e., the stress and strain fields are both functions of the transient temperature distribution, while the effect of the stress and strain field on the temperature is negligible, the problem may be decomposed into a purely thermal, and thermo-mechanical analysis. As stated above, effects of the method of clamping on both analyses are investigated as well as the effects of operating at varying distances from a free or clamped edge. Figure 2 shows a schematic of the model considered where straight line laser paths parallel to the clamped or free edge at perpendicular distances, a, are examined. It is assumed that at sufficiently large values of a, both the thermal and mechanical fields are unaffected by the presence of the clamped or free edge. However, as the distance of operation is reduced, there will be some threshold value of a where the presence of that discontinuity will cause a perturbation in the behavior of the model. In fact there will be two distinct operational regions, excluding the unperturbed case. One where the mechanical field will be affected while the thermal field remains unaffected, and a second at an even smaller distance where there will be a coupling of effects due to both the mechanical and thermal field "feeling" the presence of the discontinuity in material. This is a central concept in terms of analysis, as this enables the isolation and study of purely mechanically induced behaviors as long as the process is operating at distances greater than the threshold. It is expected that the mechanical field will be perturbed well before that of the thermal field. Practically, this further seems logical as plastic deformation in the laser forming process occurs on a relatively short time scale. This serves to further decrease the effective thermal threshold distance for single scan applications. However, the cooling phase will be affected by the presence of the insulated edge, and will have implications for multiple scan applications, where the thermal field from previous scans may need to be taken into account for future ones. The case of highly thermally conductive clamps is also addressed.

3 Experimental Conditions

Experiments were conducted with a CO_2 laser with a maximum 1500 W power output, with a Gaussian intensity distribution. The assumption of a Gaussian distribution, although not exact, is a widely accepted approximation. The laser system remained stationary while a precision XY platform translated the specimens along the desired straight path and velocity. Edge-clamped specimens were clamped at one end cantilevering the specimen (Fig. 1). The clamp material in contact with the specimen is of low thermal conductivity as to inhibit enhanced conduction keeping the thermal field comparable to that of the unclamped case. The unclamped specimens were supported from underneath by a low conductivity wood block (Fig. 1). The temperature gradient mechanism is the dominant mechanism for all the presented work.

All specimens are square 80 mm edge length, 0.89 mm thickness coupons of low carbon steel AISI 1010. Samples are treated to remove surface inconsistencies and then coated with graphite to enhance laser power absorption. Constraint induced phenomenon are of central interest for the current study, requiring isolation of the distance to the free or clamped edge, and the clamping method as the only variable parameters. All specimens are subjected to an applied power of 800 W at a beam spot diameter of 4 mm, at a velocity of 50 mm/s along a straight scanning path. Both the clamped and free specimens were run at distances of 40 mm (center scan), 25 mm, and 10 mm from the free or clamped edge. Both single and multiple scan (five total) experiments were conducted. In the case of multiple scans, the scanning path direction remained constant with a 4 min cooldown stage between scans. No forced cooling was employed to aid in either the cooldown stage between scans or during the scans themselves. Local deformations including bending angles for both the single and multiple scan cases were determined through the use of a coordinate measuring machine.

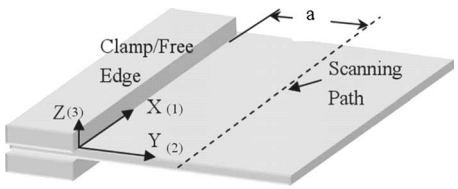

Fig. 2 Schematic of clamped specimen specifying coordinate system and operating distance

4 Numerical Analysis

For this research, both the rigidly constrained (edge-clamped) and free (unclamped) cases were modeled. As this is a coupled thermo-mechanical analysis, both thermal and mechanical constraints are required. It is assumed, however, that the coupling is sequential. This enables solving the thermal model independently, and using the solution data (transient temperature distributions) as inputs to the mechanical model.

For the thermal model, both clamp-type models are subjected to the same surface/boundary conditions; convection is specified on all plate surfaces, while a moving circular heat source with a Gaussian power distribution specified by a user defined FORTRAN script simulates the effect of the laser. The temperature dependence of thermal conductivity and specific heat is also taken into account. The governing equation is therefore the temperature dependent classical heat equation with convective sources:

$$\rho \cdot C_p(T) \cdot \frac{\partial T}{\partial t} = \nabla(k(T)\nabla T) + \sum h_i(T - T_\infty) \tag{1}$$

The mechanical models take into account both the dynamics of the process and nonlinear geometric effects stemming from large deformation theory. The temperature dependence of material properties including Young's modulus, coefficient of thermal expansion, and flow stress are taken into account as well. It is assumed that the total strain and strain rate may be decomposed into elastic, plastic, creep, and thermal components of strain and strain rate in an additive manner by: $\dot{\varepsilon}_{tot} = \dot{\varepsilon}_{el} + \dot{\varepsilon}_{pl} + \dot{\varepsilon}_{th}$ where the contribution from creep is not considered due to the relatively short time scale over which deformation occurs. Flow stress is also modeled with a dependence on strain and strain rate. Elastic strains are calculated through an isotropic Hooke's law, whereas the onset of yielding in the simulations is determined by the Von Mises criterion:

$$[(\sigma_1-\sigma_2)^2+(\sigma_2-\sigma_3)^2+(\sigma_1-\sigma_3)^2]/2=\sigma_y^2 \quad (2)$$

where σ_y is the temperature dependent flow stress determined from a uniaxial tension test. Further, the resultant plastic strain is governed by the flow rule:

$$d\varepsilon_{ij}=d\lambda\frac{\partial f}{\partial\sigma_{ij}} \quad (3)$$

where σ is stress, ε is strain, $d\lambda$ is the instantaneous proportionality constant, and $f=f(\sigma_{ij})$ is the yield function. In this case, the Von Mises criterion is used as the appropriate yield function $f(\sigma_{ij})$.The strain dependence of flow stress is modeled as:

$$\sigma_y=K\varepsilon^n \quad (4)$$

where K is the strength coefficient, and n the strain hardening component. Strain rate dependence of flow stress is given by

$$\sigma_y=C\dot{\varepsilon}^m \quad (5)$$

where C is the strength coefficient, and m is strain rate sensitivity exponent, also a temperature dependent parameter. Although the strain hardening and rate sensitivity components may be determined analytically, the empirical relationships suggested by Vashchenko et al. [13] and Maekawa et al. [14] have been adopted as they directly incorporate temperature, strain, and strain rate dependence:

$$\sigma_y=\sigma_s+(8.2+1.3\varepsilon\cdot e^{-0.0135\cdot\varepsilon})\cdot(0.97e^{0.0007\cdot\dot{\varepsilon}})\cdot(1.14-0.0023\cdot T) \quad (6)$$

for $293\ \mathrm{K}<T<573\ \mathrm{K}$, where σ_s is the static flow stress at 293 K, and

$$\sigma_y=A(T,\dot{\varepsilon})\cdot\left(\frac{\dot{\varepsilon}}{1000}\right)^{0.0195}\cdot\varepsilon^{0.21} \quad \text{for} \quad T>573\ \mathrm{K} \quad (7)$$

where

$$A(T,\dot{\varepsilon})=1394e^{-0.00118\cdot T}+339\cdot\exp\left\{-0.0000184\cdot\left[T-\left(943+23.5\cdot\ln\frac{\dot{\varepsilon}}{1000}\right)\right]^2\right\} \quad (8)$$

Implementation of these material property relationships within the simulation is accomplished through the use of a temperature and strain rate dependent yield stress ratio:

$$R(T,\dot{\varepsilon})=\frac{\overline{\sigma}}{\sigma_s} \quad (9)$$

where $\overline{\sigma}$ is the strain rate dependent flow stress. The strain and temperature dependence is first taken into account and then multiplied by the appropriate yield stress ratio for the rate dependent effect.

Numerical models contain between 2400 and 4200 20-node quadratic elements; DC3D20 for the thermal case, and C3D20 for the mechanical case in ABAQUS. These higher order elements, although more computationally expensive, prevent shear locking and hourglass effects associated with their eight-node counterparts, and are therefore necessary for this, a bending-dominated deformation process [15]. Attention is given to specifying a fine mesh resolution at and near the scanning path, while away from the scanning path there is a fairly coarse mesh density.

The clamped case requires the specification of zero displacement in the Y and Z direction along one full edge, and restriction of X displacement at one additional node at the center of the scan path at the bottom of the plate to inhibit rigid body motion. The decision to constrain only the Y and Z displacements is due to the fact that although there is some constraint in the X direction, it is well below that of the Z, whereas the Y restriction serves as a reference about which the entire part may expand or contract. This is supported by Postaciaglu et al. [16] who specifically address this point. Furthermore, models including a constraint in the X direction were unable to capture several experimentally observed trends.

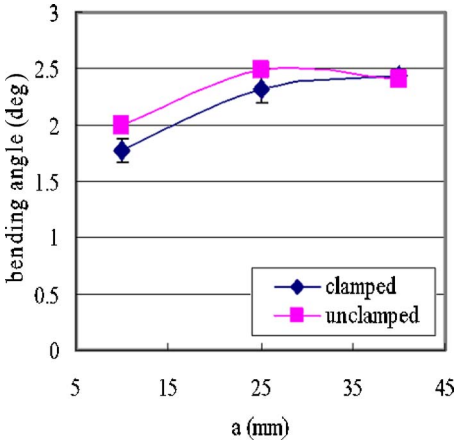

Fig. 3 Experimental, average bending angle as a function of operating distance (Q=800 W, v=50 mm/s)

The unclamped case requires that only rigid body displacement and rotation be constrained as it is attempting to simulate an essentially unconstrained condition. This is accomplished by specifying zero X, Y, and Z displacement on two nodes located at the center of the laser scanning path at the midplane and bottom surface. This constrains X, Y, and Z rigid body displacement, and rotation about the X and Y axes. One further node, located at the end of the scanning path on the bottom plane, is constrained to zero displacement in the Y direction to inhibit rotation about the Z axis.

5 Results and Discussion

Simulations were performed at each of three velocities, v=50, 60, and 70 mm/s, for three different powers, Q=640, 800, and 960 W and three distinct operational distances a=10, 25, and 40 mm for both the clamped and unclamped cases. Figures 3–8 show representative experimental and numerical results for both the average bending angle magnitude, and bending angle distributions. It is seen that both the experimental magnitudes and trends are captured by the numerical results. Upon this validation of the numerical model, several more sets of simulations were run at two additional velocities and powers.

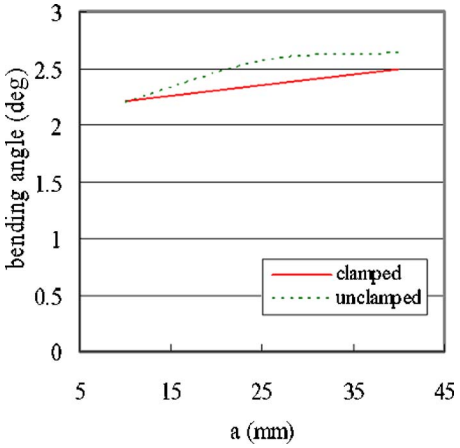

Fig. 4 Numerical, average bending angle as a function of operating distance (Q=800 W, v=50 mm/s)

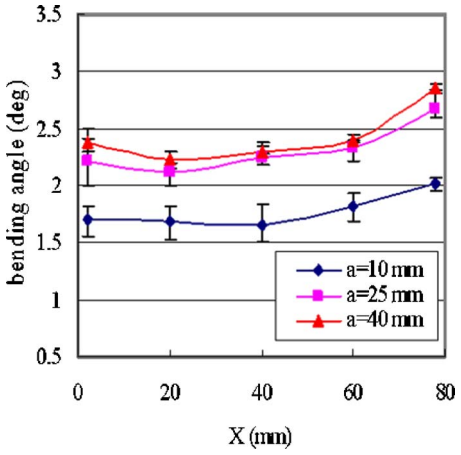

Fig. 5 Clamped, experimental bending angle distribution (Q =800 W, v=50 mm/s)

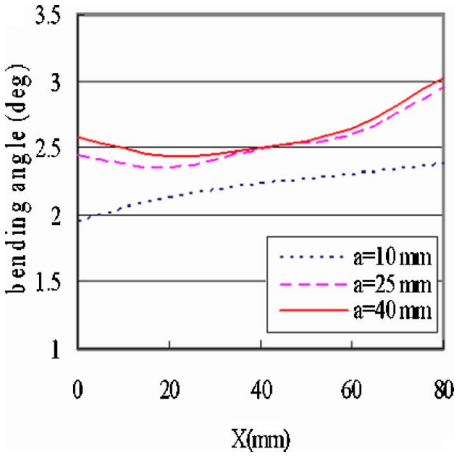

Fig. 8 Unclamped, numerical bending angle distribution (Q =800 W, v=50 mm/s)

5.1 Average Bending Angle. Both the average bending angle and the bending angle distribution along the laser scan path are affected by the operating distance to the clamped or free edge. Beginning with the former, it is seen in Figs. 3 and 4 that for both the clamped and unclamped cases, the average bending angle decreases with decreases in operating distance. The figures also depict the slope of the bending angle function for both cases exhibiting a dramatic change as the distance a decreases from 25 to 10 mm, as opposed to the functional behavior between 40 and 25 mm. This therefore represents a transition, with respect to the average bending angle, from the unperturbed situation to one where the presence of the clamped or free edge is "felt" in a mechanical sense. It will be shown in subsequent sections that this is a purely mechanical phenomenon as the thermal field remains unchanged on the time scale over which deformation occurs.

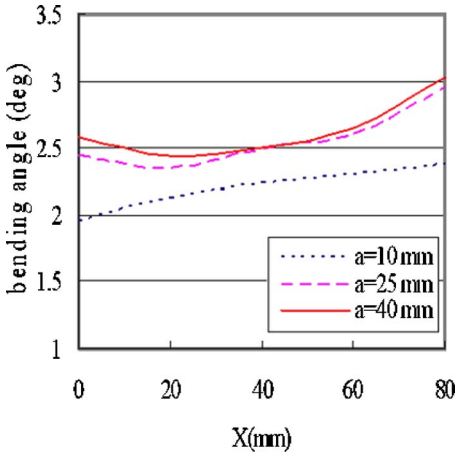

Fig. 6 Clamped, numerical bending angle distribution (Q =800 W, v=50 mm/s)

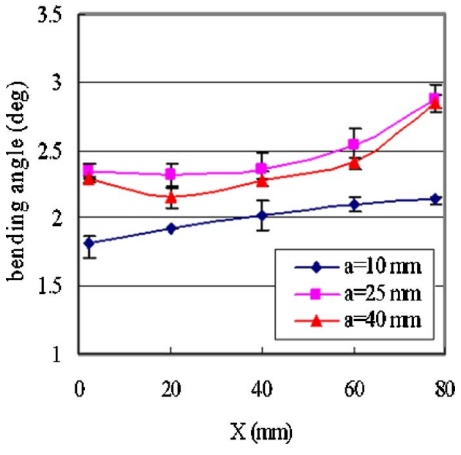

Fig. 7 Unclamped, experimental bending angle distribution (Q=800 W, v=50 mm/s)

In examining the mechanical aspects of the process, it is important to distinguish between two types of mechanical constraint. The first is an inherent mechanical constraint due purely to the geometric characteristics of the part. It is well established that plastic strain along the direction perpendicular to the scan path is directly linked to the magnitude of the average bending angle and is caused by the locally heated volume of material being constrained by the relatively cold surrounding material. The extent to which this cold material inhibits local thermal expansion is the level of inherent constraint being applied to the heat affected zone. A larger level of inherent constraint will result in enhanced plastic strain in the Y direction and therefore an increase in local, and average bending angle. The second is an applied external constraint provided, for example, by the presence of an edge clamp. It will be seen that for operation within the presented processing window, inherent constraint plays the dominant role in governing the final average bending angle magnitude, while the external constraint, effectively, plays almost none at all.

The decrease in average bending angle as the operating distance reduces is due to a decrease in the inherent constraint (in the Y direction) as a free or clamped edge is approached. The reason for this reduction in constraint stems from the fact that the edge being approached is traction free. Therefore, instead of a large volume of material providing a relatively rigid surrounding, the material adjacent to the traction free surface now is able to expand much more freely. This in turn results in less plastic strain and therefore a lower bending angle. The metric chosen to express this reduction in constraint is the instantaneous spatial integral of the elastic normal stress distribution in the Y direction (σ_{yy}). This integration is performed along a path perpendicular to the scanning direction at a typical interior section at the instant the laser passes this location. Further, only the compressive components of stress are taken as a measure of inherent constraint, as this is de facto what is providing the resistance to thermal expansion at that particular instant. Figure 9 shows a typical plot of σ_{yy}, or constraint, as a function of Y for three different operating distances. It is obvious from the plot that the total component of compressive (integral of the negative portions of the curve) normal stress decreases as

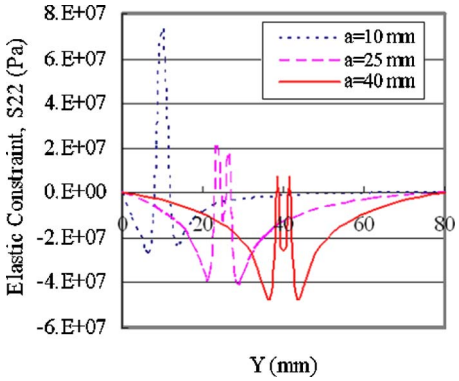

Fig. 9 Comparison of elastic constraint for three operating distances (unclamped, Q=960 W, v=70 mm/s)

operational distance decreases. It is seen from Figs. 10 and 11 that within the process window of parameters simulated, the elastic constraint for both the unclamped and unclamped cases decreases monotonically with: decreases in operating distance, decreases in power, and increases in velocity. Figures 12 and 13 show the average bending angle decreasing monotonically in the same manner as that of the elastic constraint with respect to changes in operating distance, power, and velocity. This suggests that changes in inherent constraint with respect to changes in process

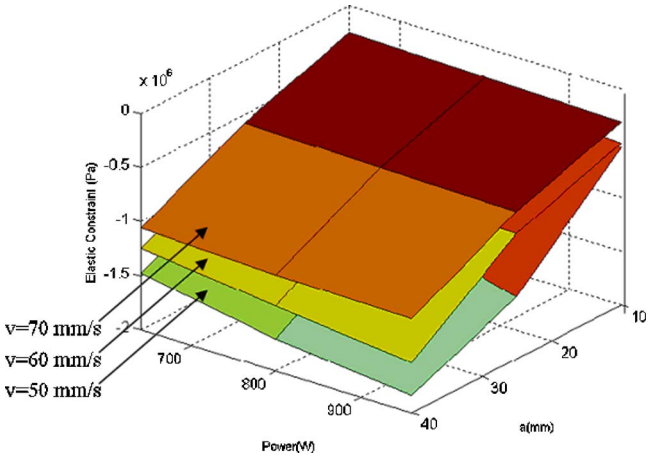

Fig. 10 Clamped, elastic constraint as a function of power and operating distance for three velocities

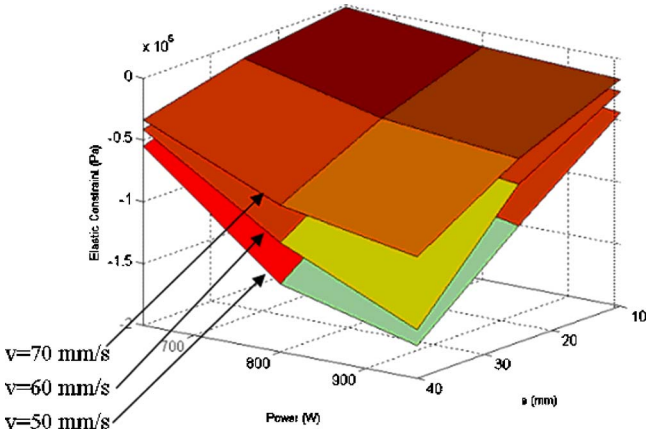

Fig. 11 Unclamped, elastic constraint as a function of power and operating distance for three velocities

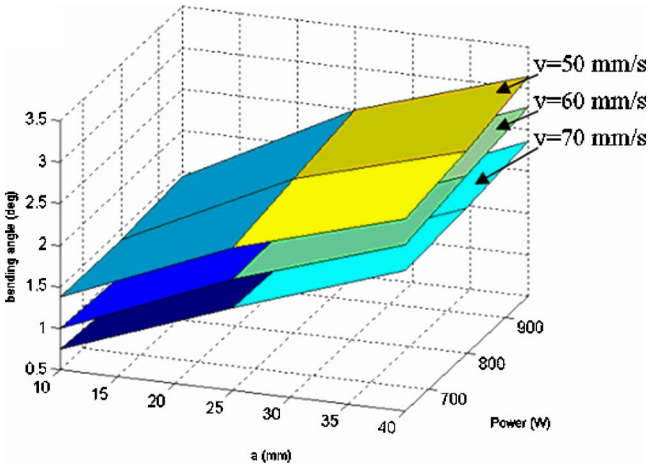

Fig. 12 Clamped, numerical, average bending angle as a function of operating distance and power for three velocities

parameters is a valid explanation for the observed behavior in average bending angle magnitude for both the clamped and unclamped cases.

A comparison between the clamped and unclamped cases may also be made. Figure 14 shows a typical plot of σ_{yy} vs Y for the clamped and unclamped cases operating at the same powers, velocities, and distances from the edge. It is seen that the stress distributions remain consistent until the clamped edge is approached. This deviation is an added stress due to the Poisson's effect stemming from the presence of the clamp, which acts to inhibit displacement in the Z direction thereby increasing stress in the Y direction. This would suggest that the presence of this external constraint would act to increase the total level of constraint, thus causing an increase in bending angle. However, it is seen that although the clamped specimens have much higher constraint values, the average bending angles for the unclamped configuration are greater in many cases. This is clarified by the following explanation. Although there is an increase in externally applied constraint, the presence of the clamp also introduces a competing effect by increasing the effective bending rigidity about the X axis. This is seen by examining the instantaneous σ_{yy} distribution at the bottom surface of the specimen as the laser passes this location. Figure 15 shows a dramatic increase in elastic constraint magnitude (left scale, top surface) for the clamped case relative to the unclamped as the operating distance is decreased. However, Fig.

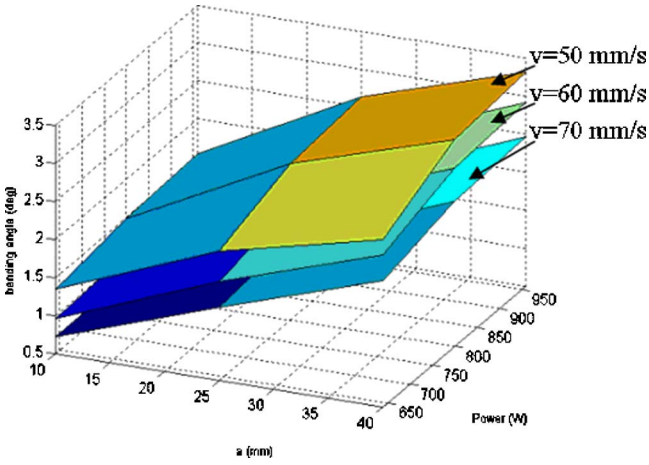

Fig. 13 Unclamped, numerical, average bending angle as a function of operating distance and power for three velocities

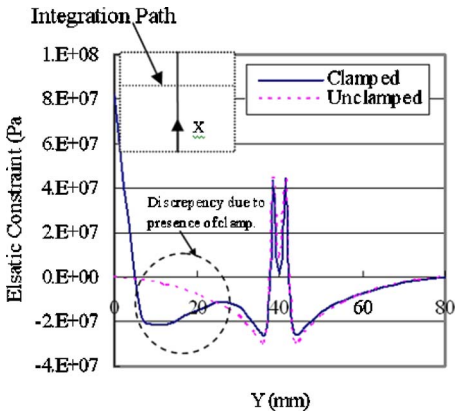

Fig. 14 Comparison of clamped and unclamped σ_{yy} (constraint) distribution (P=800 W, v=60 mm/s, a=40 mm)

15 also shows a corresponding increase in instantaneous tensile σ_{yy} (right scale) across the part in the bottom surface of the clamped specimen, while the corresponding surface in the unclamped model is traction free. These competing effects introduced by the presence of the clamp provide an explanation for the above-mentioned discrepancy between the clamped and unclamped cases in average bending angle magnitudes.

5.2 Bending Angle Distribution. Bending angle distribution refers to the variation in local bending angle along the laser scan path. Referring back to Figs. 5–8, it is seen that for both the clamped and unclamped bending angle distributions, the interior portions of the scan path have a smaller magnitude slope than those of the entrance and exit portions of the function. This is due to edge effects induced by free edges perpendicular to the laser scanning path.

The bending angle is calculated from relative Z displacements along paths at fixed Y distances from, and parallel to, the laser scan path (Fig. 16). The locations of these paths relative to the scan path are chosen to lie outside of the heat affected zone so as to avoid any local distortions, and are the same for both the clamped and unclamped cases for each distinct operating distance. The total local bending angle is calculated from the addition of the two angles generated on either side of the scanning path. The

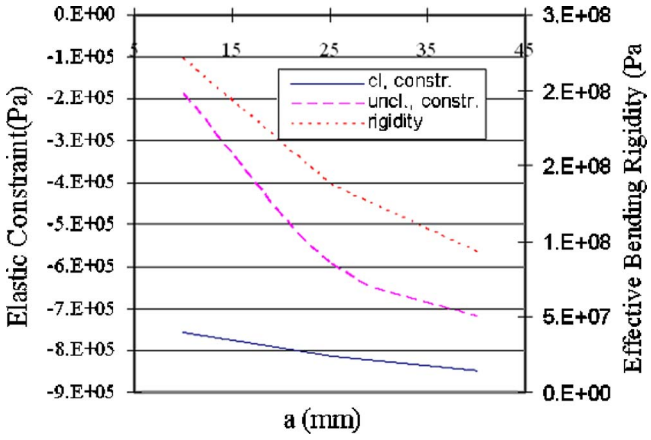

Fig. 15 Typical comparison of total elastic constraint in the top surface between clamped and unclamped configurations (left scale) (Q=800, v=60 mm/s). Also shown is the instantaneous stress at the bottom layer of the part, showing a dramatic increase in effective bending rigidity as operating distance decreases (right scale).

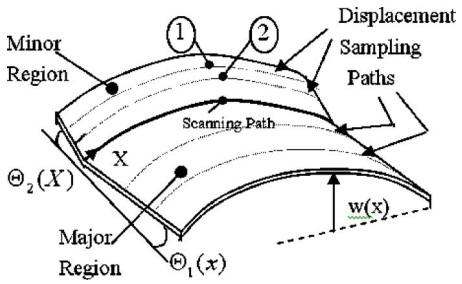

Fig. 16 Portrayal of major and minor regions, sampling path locations, major and minor bending angles, and local Z displacement $w(x)$

volume of material adjacent to the clamp, or for unclamped cases, the smaller section, will be termed the minor region, and the other, the major.

The metric chosen to quantify the variation in bending angle is the curvature of the bending angle vs X function, and will be referred to as bending angle curvature. Bending angle curvature is approximated by fitting a second order polynomial through the desired function, then using the coefficient of the quadratic term as the quantifier, i.e., the second derivative of the function. It is important to note that the variation in bending angle is not equivalent to the variation in displacement along the part. The bending angle curvature function is a measure of the *relative* curvatures in Z-displacement vs scan distance along sampling paths. Therefore, an increase in the difference in curvatures between displacement vs X along sampling paths results in an increase in bending angle curvature, and thus greater variation in local bending angle along the scan path. The sign of curvature refers only to the curvature direction, with a concave down instance being arbitrarily chosen as negative.

In order to isolate the effects of changes in operating distance, the unclamped case will first be examined to exclude the effects of any external constraint. Figure 17 is a typical plot of bending angle curvature as a function of operating distance. It is seen that for both the clamped and unclamped cases, curvature strictly increases with increases in operating distance for both the clamped and unclamped cases. The slope of the curvature function for both cases also exhibits a dramatic change as the distance "a" is decreased from 25 to 10 mm, as opposed to the functional behavior between 40 and 25 mm.

The variation in Z displacement as a function of X is due to bending about the Y axis induced by elastic and plastic strains in the X direction, as well as nonuniform plastic strain in the Y direction along the scanning path. Upon consulting the numerical results, it is seen that the former has a minimal effect on the final

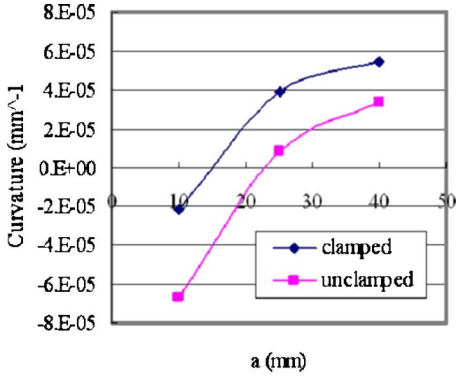

Fig. 17 Representative curvature comparison between clamped and unclamped configurations (Q=640 W, v=60 mm/s)

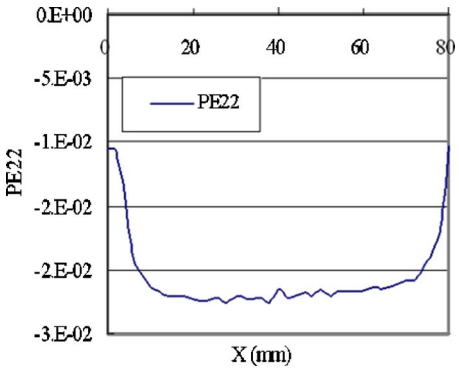

Fig. 18 Plastic strain in the *Y* direction as a function of *X*. Note the decrease in magnitude at both edges.

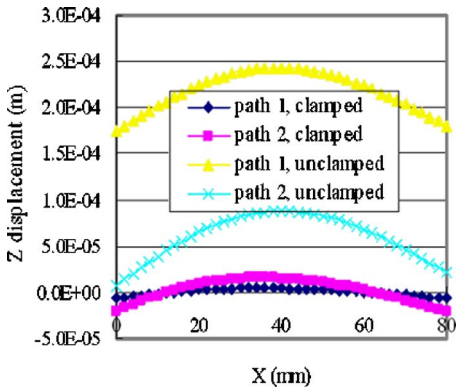

Fig. 19 (Numerical results) Comparison of relative displacement curvatures in minor region. Sampling paths are defined in Fig. 10 (a=40 mm, Q=640 W, v=60 mm/s).

Z displacement, as the total X strain ($d\varepsilon_{el}+d\varepsilon_{pl}$), remains relatively constant through the thickness of the part, and thus contributes mostly to a uniform shrinkage in the X direction. The latter is therefore the major contributor to variations in Z displacement along sampling paths. The change in plastic strain in the Y direction as a function of X (Fig. 18) along the scan path is again due to changes in inherent constraint. However, as opposed to the average bending angle study, the distribution is affected by changes in constraint due to the presence of the edges *perpendicular* to the scanning path. Upon entering or exiting (X=0, and X=W, respectively) the part, the volume of material heated by the laser experiences much less constraint due to a reduced volume of surrounding "cold" material. Bao and Yao [3] have also specifically examined variations in deformation along the scan path, and attributed them to thermal effects resulting from the presence of the two free edges perpendicular to the scan. For example, the peak temperature at the starting free edge is lower than that of the quasi-steady peak and the peak temperature at the end of the scan is much greater due to heat accumulation. However, thermal simulations suggest that the presence of the clamped or free edge does not have an effect on the local temperature distribution. In fact, the local temperature distributions on the time scale over which deformation occurs are identical for each of the a=40, 25, and 10 mm cases. Subsequent sections of this paper address thermal considerations in detail.

The functional dependence of displacement curvature on operating distance is also explained by changes in inherent constraint, as according to numerical results, plastic and elastic strain in the X direction along the scanning path are not functions of operating distance, and remain constant. As explained in the previous section on average bending angle, a decrease in operating distance results in a decrease in constraint due to the presence of a free edge parallel to the scanning path, and therefore a reduction in plastic strain in the Y direction. In this case, the reduction in constraint due to the presence of a free edge parallel to the scanning path *relative* to the reduction in constraint due to the edges perpendicular to the scanning path is the source of the functional dependence. For example, the a=10 mm, and a=40 mm cases have effectively the same reduction in constraint due to the edges perpendicular to the scanning path. However, the a=10 mm case is associated with a much reduced quasi-steady level of inherent constraint due to the proximity of the free edge parallel to the scan path. This reduction in relative difference in inherent constraint results in a smaller variation in Z displacement along paths parallel to the scanning path and therefore reduces the bending angle curvature.

The clamped case may be explained through the same line of reasoning as that of the unclamped. Again, plastic and elastic strains in the X direction are constant through the part thickness, are not functions of operating distance, and are equal to those of the unclamped cases. This is due to the fact that the clamp mainly serves to inhibit Z displacement. Figure 17 also serves as a typical plot, and shows that bending angle curvature in the clamped case is greater than its unclamped counterpart for all operating distances. This may again be explained by differences in relative displacement curvatures. Figure 19 shows a typical plot of Z displacements along sampling paths in the minor section for the 40 mm operating-distance case. It is seen that the presence of the clamp greatly inhibits not only displacement magnitude but *variation* in displacement as well, particularly for the sampling path closer to the clamp. Although the displacements have been greatly reduced, the difference in displacement curvature has increased substantially, thus causing a higher bending angle curvature than that of the unclamped case. Numerical results also indicate that bending angle curvature for both the clamped and unclamped cases increases monotonically with: increases in operating distance, increases in power, and decreases in velocity.

5.3 Extension to Multiple Scan and Thermally Conductive Clamp Applications. Although the above analysis was restricted to single scan processes, the concepts are extendable to multiple scan applications. Although local increases in elastic modulus may hamper the effects slightly, the strain hardening effects caused by successive scans should not play a large role in terms of the factors influencing process dependencies on inherent and externally applied constraints, as these are purely geometric. The applied thermal field will be affected by the chosen method of clamping and magnified for an increased number of laser scans in terms of changes in power distribution within the laser spot due to part deformation. This effect is negligible for low numbers of laser scans as suggested by Edwardson et al. [8]. The multiple scan results presented are constrained to five scans total, well below the number of scans required for deviation from the idealized circular Gaussian distribution. One other thermal consideration that may be required to be taken into account is the effect of heat accumulation on "long-time" temperature distributions introduced by asymmetric thermal conditions with respect to the location of the scan path. As mentioned in the overview, the local temperature distributions on the time scale over which deformations take place are unaffected by the presence of a thermally insulated boundary, although the temperature time history in the cool down phase will be. This time history affect will have implications for multiple scan applications, where the thermal field from previous scans may need to be taken into account for future ones. Figure 20 shows the numerically predicted temperature distributions about the scanning path for three operating distances for a single scan. Please note that the temperature distributions in Figure 20 are taken at times to accentuate the asymmetries, and not at the instant the laser is passing that location. It should also be noted that curves in the figure are limited to Y distances that are symmetric about the scan location, and not across the entire

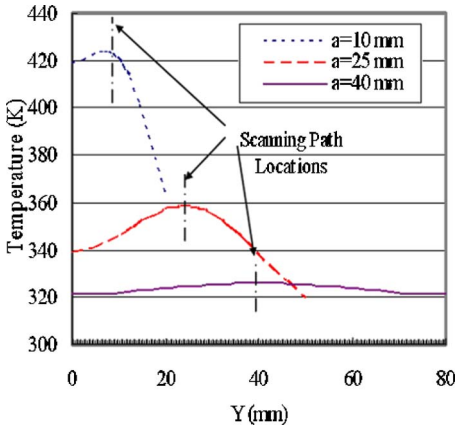

Fig. 20 Comparison of temperature distribution for three operating distances (numerically obtained). *Note*: Distributions taken at times accentuating asymmetries.

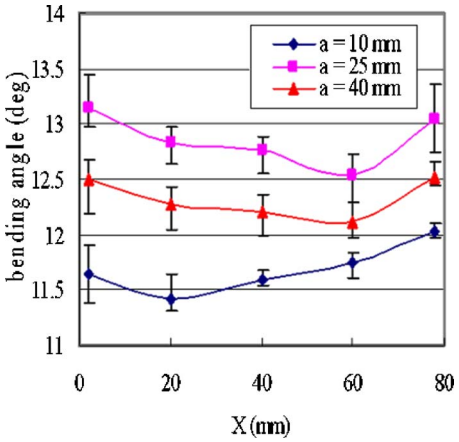

Fig. 22 Clamped-multiple scan, experimental bending angle distribution (*Q*=800 W, *v*=50 mm/s)

plate. It is seen that, as one might expect, the 10 mm case is highly asymmetric while the asymmetries decrease with increases in operating distances, with a perfectly symmetric distribution for the 40 mm case. Besides causing an asymmetry, the presence of the insulated boundary also acts to increase the time required in cooling down to ambient temperature, again influencing the time chosen between successive scans.

Figures 21–23 show experimentally obtained results for average bending angle magnitude and bending angle distribution for a total of five scans. It is seen that the bending angles have increased. However, curvature magnitudes (not shown) for the 25 and 40 mm operating distances have changed only slightly, while the 10 mm case has seen a large increase in curvature magnitude. This suggests that only curvature magnitude and not direction may be altered through the use of successive scans. The average bending angle as a function of operating distance also follows the same trend in that a decrease to a 10 mm operating distance causes a substantial decrease in average bending angle.

The effects of introducing a clamp with a highly enhanced thermal conductivity were also considered. Figure 24 shows the temperature time history at a typical location on the scanning path, away from the perpendicular free edges for both the insulated and conductive configurations at a 10 mm operating distance. Also on the plot is the plastic strain in the *Y* direction at the same location as a function of time for a 10 mm operating distance. It is seen that the temperature time history, including peak temperature, is unaffected until sufficient time has past where one observes a slightly enhanced cooling effect provided by the conductive clamp which acts as a heat sink. However, this divergence from the insulated case occurs at a time when the corresponding plastic strain has already reached a steady state, suggesting that the presence of the conductive clamp will not play a role in the behavior of the process for single scan applications. However, a further

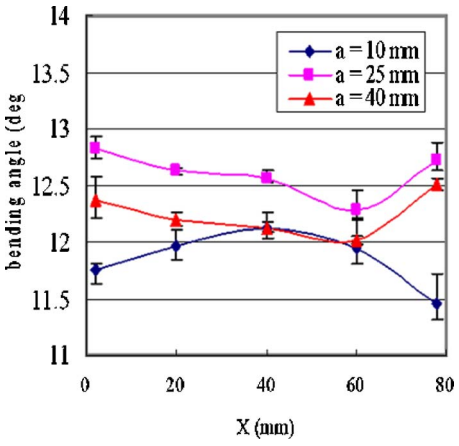

Fig. 23 Unclamped-multiple scan, experimental bending angle distribution (*Q*=800 W, *v*=50 mm/s)

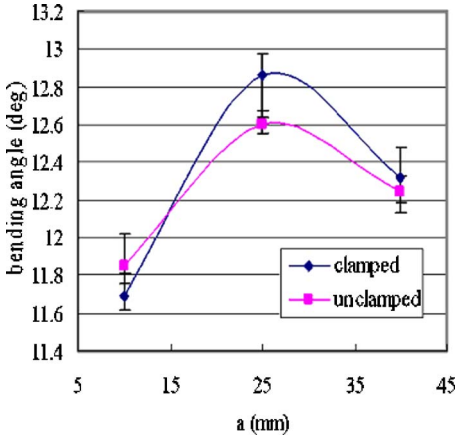

Fig. 21 Multiple scan, experimental average bending angle (*Q*=800 W, *v*=50 mm/s)

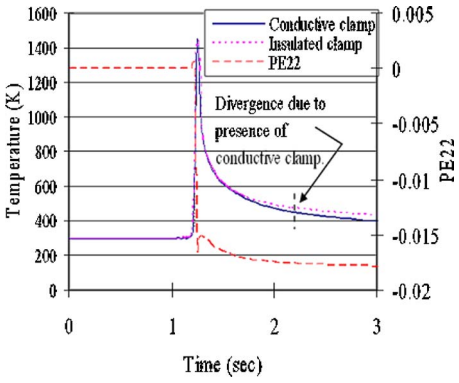

Fig. 24 Comparison of temperature time histories between the insulated and highly conductive clamp case. Also shown is plastic strain PE22 in the *Y* direction (right scale) (*a*=10 mm, *Q*=800 W, *v*=50 mm/s).

decrease in operating distance or a multiple scan application may require the effects of the thermal properties of the clamp to be taken into account.

5.4 Further Analysis. To further understand the effect of the operating distance, a, on the thermal field resulting from the laser scan, an analytical approach incorporating the method of images is employed here. It is well established that the heat transfer process describing the laser forming process is dominated by heat conduction within the part and surface convection at the boundaries. It is assumed that the thermo-mechanical response is sequentially coupled in that the mechanical field is driven by the temperature distribution, while the thermal field is essentially unaffected by the plastic deformation in the part. The analytical formulation below also does not take into account the temperature dependence of the thermal properties. Also, as this is a 2D formulation, this is not meant to serve as an aid in predicting bending as no calculation of temperature gradients through the thickness may not be calculated. Although there is some sacrifice in terms of numerical accuracy, it does provide valuable qualitative information about the transition from a steady state symmetric temperature distribution, to an asymmetric one due to the presence of an effectively thermally insulated boundary. Therefore, the governing equation for the process is the classical transient heat equation, including convective terms:

$$\frac{\partial^2 T}{\partial x^2} + \frac{\partial^2 T}{\partial y^2} = 2\lambda \frac{\partial T}{\partial t} + \frac{PH}{A}(T - T_\infty) \tag{10}$$

where $1/2\lambda$ is the thermal diffusivity, P the perimeter, A the cross-sectional area, and H, the heat dissipation ratio which is actually h/k, where h is the convective heat transfer coefficient and k is thermal conductivity. This study is restricted to thin plates, facilitating the use of the 2D heat equation. Rosenthal [17] suggests a solution for this case by introducing a parameter, $\xi = x - vt$, a local coordinate that remains fixed with the source as it traverses the domain, thereby introducing the "quasi-stationary" condition and eliminating the time dependence at sufficiently large distances from free edges perpendicular to the scanning path. Employing a polar coordinate parameter, $r = \sqrt{\xi^2 + y^2}$ the solution is given by:

$$\Theta = \frac{\alpha Q}{\pi k g} e^{-\lambda v \xi} K_0 \left[\left(\lambda^2 v^2 + \frac{2H}{g} \right)^{1/2} r \right] \tag{11}$$

where g is the sheet thickness, α is the power absorption coefficient, v is the laser velocity, and the coefficient 2, in front of H, takes into account convective losses for both the top and bottom surfaces.

The solution is further developed by using the method of images, to simulate thermally insulated boundaries on surfaces parallel to the direction of the moving source, effectively modeling a finite plate in two directions, not just one. This solution is limited, however, in the sense that it is only capable of modeling a symmetric temperature distribution with respect to the heat scanning path, as the point source is kept equidistant between the two simulated insulated boundaries. Below, the authors suggest a means for using the method of images in a similar manner, but enabling the modeling of an asymmetric temperature distribution.

Rosenthal's method of images involved reflecting a single source through an infinite number of planes located at integral multiples of the desired distance to an insulated edge. This may be extended to the reflection of a double point source as well (Fig. 25). This solution for a dual source separated by a fixed finite distance $2a$:

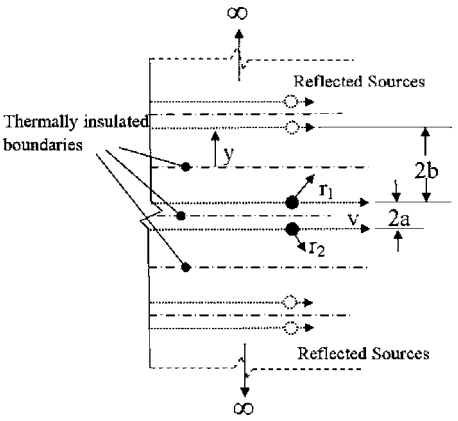

Fig. 25 Schematic representation of dual source reflection process in analytical formulation

$$\Theta = \frac{\alpha Q}{\pi k g} e^{-\lambda v \xi} \left[K_0 \left(\sqrt{(\lambda v)^2 + \frac{2H}{g}} r_1 \right) + K_0 \left(\sqrt{(\lambda v)^2 + \frac{2H}{g}} r_2 \right) \right] \tag{12}$$

may be reflected an infinite number of times about planes located at integral multiples of the distance b. Since "a" does not necessarily equal "b," this imposes thermally insulated boundaries at a distance a from one side of the source and b from the other, thereby simulating the desired asymmetric temperature distribution caused by laser operation in close proximity to one free edge parallel to the direction of the source. The solution representing this reflection is characterized by:

$$\Theta = \sum_{n=-\infty}^{\infty} \frac{\alpha Q}{\pi k g} e^{-\lambda v \xi} \left[K_0 \left(\sqrt{(\lambda v)^2 + \frac{2H}{g}} r_{1,n} \right) + K_0 \left(\sqrt{(\lambda v)^2 + \frac{2H}{g}} r_{2,n} \right) \right] \tag{13}$$

$$r_{1,n} = \sqrt{(\xi^2 + (y + (2n-1)b + (n-1)2a)^2} \tag{14}$$

$$r_{2,n} = \sqrt{(\xi^2 + (y + (2n-1)b + 2na)^2} \tag{15}$$

Figure 26 shows the analytically predicted transition from a symmetric temperature distribution about the scan path to an asymmetric one as the operating distance decreases from 25 to 5 mm. It is seen that the 25 mm case is totally undisturbed by the presence of the insulated boundary by observing the 400 K isotherm has retained a "regular" shape, and therefore any distance greater than 25 mm will also retain symmetric properties. However, the 10 mm case begins to exhibit some asymmetries in that its 400 K isotherm has now merged with the insulated boundary representing an increase in the volume of heated material, but may not necessarily have a large impact on final deformation. The 5 mm case, however, shows that the 720 K isotherm is no longer a regular shape, and the 600 K isotherm has completely merged with the insulated boundary suggesting considerable asymmetries which would have an impact on final deformation. It also follows that for a maximum perturbed isotherm temperature associated with a given operating distance, all temperatures less than this maximum will also be perturbed, and will so to a greater extent. Also worth noting is Vollertsen's [18] calculation of a critical isotherm on the order of 600 K as a geometric boundary for the plastic zone in steel. This would further imply that at distances less than 10 mm, the presence of the insulated edge must be taken into account in application. This also represents the threshold distance discussed earlier for transition from purelymechanically induced perturbations to coupled thermo-mechanical effects due to the presence of

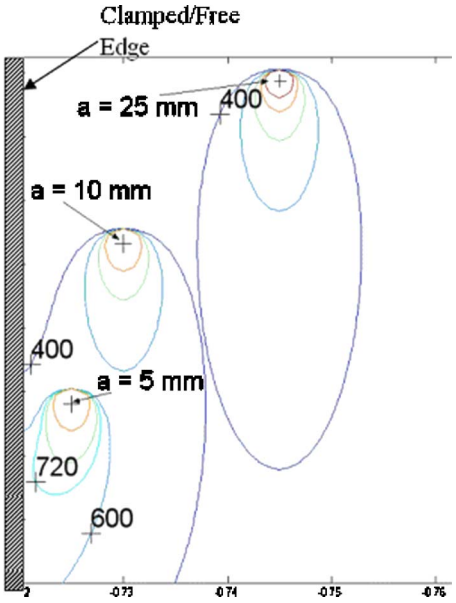

Fig. 26 Contour plot for selected operating distance. Note the transition to an asymmetric temperature distribution with respect to the scanning path (analytically obtained).

the clamped or free, but thermally insulated edge.

6 Conclusion

The results of the analysis presented suggest that the presence of an external constraint such as a clamp, as well as the operating distance with respect to a clamped or free edge, do have implications on the final deformation of a thin sheet specimen. Referring to the average bending angle portion of the study, the presence of the constraint, although relevant, results in two competing effects thereby offsetting each other and resulting in almost no significant change in final deformation. However, the effect of operating in close proximity to a clamped or free edge will have dramatic effects on final deformation and should be taken into account in application. Similarly, for bending angle distribution, the operating distance will have a considerable effect on the final variation in bending angle along the scanning path. The presence of the clamp will also serve to change the bending angle distribution by increasing the relative displacement curvatures and thereby causing larger variations compared to the unclamped configuration. In contrast to single scan applications, the thermal fields from successive scans may need to be taken into account when predicting final deformation characteristics for both the insulated and conductive clamp cases. Further investigation is required to determine the nature of these effects.

Acknowledgment

This work is supported in part by NIST under Grant No. ATP #00005269, and in part by the NSF under Grant No. DMI-0355432.

References

[1] Vollertsen, F., 1994, "Mechanisms and Models for Laser Forming, Laser Assisted Net Shape Engineering," *Proceedings of the LANE '94*, Barmberg, Germany, **1**, pp. 345–360.
[2] Mucha, Z., Hoffman, J., Kalita, W., and Mucha, S., 1997, "Laser Forming of Thick Free Plates, Laser Assisted Net Shape Engineering," *Proceeding of the LANE' 97*, Barmberg, Germany, **2**, pp. 383–392.
[3] Bao, J., and Yao, Y. L., 2001, "Analysis and Prediction of Edge Effects in Laser Bending," ASME J. Manuf. Sci. Eng., **123**, pp. 53–61.
[4] Hoffman, E. G., 1996, *Setup Reduction Through Effective Work Holding*, Industrial Press, New York.
[5] Wang, Y. W., and Pelinescu, D. M., 2002, *Prediction of Workpiece-Fixture Contact Forces Using the Rigid Body Model*, Publication source unknown.
[6] Karafillis, A. P., and Boyce, M. C., 1992, "Tooling Design in Sheet Metal Forming Using Springback Calculations," Int. J. Mech. Sci., **34**(2), pp. 113–131.
[7] Roy, U., and Liao, J., 2002, "Fixturing Analysis for Stability Consideration in an Automated Fixture Design System," ASME J. Manuf. Sci. Eng., **124**, pp. 98–104.
[8] Edwardson, S. P., Watkins, K. G., Abed, E., Bartkowiak, K., and Dearden, G., 2005, "Geometrical Influences on the Bend Angle Rate per Pass During Multi-Pass 2D Laser Forming," *Proc. IWOTE' 05, Int. Workshop on Thermal Forming*, Bremen, Germany, pp. 29–46.
[9] Jones, J. E., 2005, Internal Communications, NATechnology.
[10] Hu, Z., Kovacevic, R., and Labudovic, M., 2002, "Experimental and Numerical Modeling of Buckling Instability of Laser Sheet Forming," Int. J. Mach. Tools Manuf., **42**, pp. 1427–1439.
[11] Li, W., and Yao, Y. L., 2000, "Numerical and Experimental Study of Strain Rate Effects in Laser Forming," ASME J. Manuf. Sci. Eng., **122**, pp. 445–451.
[12] Lee, K., and Lin, J., 2002, "Transient Deformation of Thin Metal Sheets During Pulsed Laser Forming," Opt. Laser Technol., **34**, pp. 639–648.
[13] Vashchenko, A. P., Suntsov, G. N., Belalova, G. V., and Medvedev, A. A., 1991, "Mechanical Properties of Low Carbon Steel Over a Wide Range of Temperature and Strain Rates Applied to Processes of Thin Sheet Rolling," Strength Mater., **22**, pp. 1205–1214.
[14] Maekwa, K., Shirakashi, T., and Usui, E., 1983, "Flow Stress of Low Carbon Steel at High Temperature and Strain Rate (Part 2)-Flow Stress Under Variable Temperature and Variable Strain Rate," Bull. Jpn. Soc. Precis. Eng., **17**(3), pp. 167–172.
[15] Cheng, J., and Yao, Y. L., 2001, "Cooling Effects in Multiscan Laser Forming," J. Man. Proc. SME, **3**(1), pp. 60–72.
[16] Postaciaglu, N., Kapadia, P., and Dowden, J. M., 1997, "Thermal Stresses Generated by a Moving Elliptical Weldpool in the Welding of Thin Metal Sheets," J. Phys. D, **30**(16), pp. 2304–2312.
[17] Rosenthal, D., 1946, "The Theory of Moving Heat Sources and its Application to Metal Treatments," Trans. ASME, **68**, pp. 849–866.
[18] Vollertsen, F., and Rodle, M., 1994, "Model for the Temperature Gradient Mechanism of Laser Bending," *Proc. of the LANE'94*, Barmberg, Germany, **1**, pp. 371–378.